

Fabrication and Mechanical Cycling of Polymer Microscale Architectures for 3D MEMS Sensors

Mohammad Humood, Joseph Lefebvre, Yan Shi, Mengdi Han, Coleman D. Fincher, Matt Pharr, John A. Rogers, and Andreas A. Polycarpou*

Biology involves inherently complex three-dimensional designs. In addition to the geometric complexity, thin and complex biostructures composed of membranes such as insects, wings, and plants leaves can achieve complex functionalities under vibrations, such as maneuverability and resistance to strong winds, respectively. They do so by changing the shape and curvature of their membranes and ribbons. Achieving such capabilities in advanced materials would have important implications for a wide range of applications, such as three-dimensional (3D) microelectromechanical systems (MEMS), sensors, and energy harvesting devices. Such applications experience cyclic deformation up to 20–30% length compression during operation. To this end, this paper investigates mechanical cycling of a number of microscale 3D polymer-based kirigami architectures. The mechanical response of these structures revealed stable and resilient behavior equivalent to flexible natural systems upon cyclic compression up to 50% of their initial height. To understand crack formation and growth, *in situ* scanning electron microscopy (SEM) under extreme compression of 100% of their initial heights reveal internal stresses and permanent change in the curvature of the structures, resulting in the formation of cracks after 100 cycles. To enhance their fracture toughness, computational modeling, as an optimization tool is used to provide guidelines to eliminate crack growth.

1. Introduction

There is growing need to develop 3D electronic devices such as sensors, energy harvesting devices, and batteries both to improve efficiencies and to address specific requirements demanded by applications.^[1–4] Particularly, biology inherently involves 3D designs. To successfully integrate bioelectronics with biological systems, devices must adapt to the complex 3D nature of the biological systems.^[5–7] Additionally, a current approach to improving efficiency of devices is by optimizing the active materials.^[8] However, this approach often leads to higher manufacturing cost due to using advanced, high-performance materials. As an alternative approach, pop-up designs of electronics from 2D to 3D provides additional design space to improve the efficiency of these devices through the optimization of material geometry, while using inexpensive available materials in standard semiconductor fabrication.^[9] Indeed, natural systems such as insects and plants take advantage of similar complex architectures, which provides low mass, high bending stiffness, and

high cyclic reliability.^[10]

3D micro/mesostructures present an emerging route to develop new class of MEMS sensors.^[11,12] MEMS consist of devices such as sensors and actuators, together forming transducers capable of converting one form of energy to another.^[13] The development of MEMS technologies is on the rise and the MEMS market has rapidly grown surpassing \$22 billion in 2018.^[14] Nowadays, the focus for the MEMS industry is to solve issues such as reliability, to enable moving technologies from the laboratory into practical real-world applications.^[15] The operation of MEMS requires a high level of reliability^[16] of which mechanical reliability of components is critical, with fatigue representing a major failure mechanism.^[17,18] Unlike other electronic devices, MEMS are often designed to move or oscillate, with the mechanical oscillations generating an electrical output.^[19] 3D MEMS offer vastly improved bandwidth and frequency tunability over conventional 2D MEMS structures, such as cantilever beams and doubly clamped bridges.^[20,21] In a recent study, we investigated different resonant vibrational frequencies of 3D table and rotated table structures. The 3D assembled structures were found to have the ability to tune their vibrational behavior, such as natural frequencies, through

Prof. A. A. Polycarpou, Dr. M. Humood, C. D. Fincher, Prof. M. Pharr
Department of Mechanical Engineering
College of Engineering
Texas A&M University
College Station 77843-3123 TX, USA
E-mail: aploycarpou@tamu.edu

J. Lefebvre
Bruker Nano Surfaces
Eden Prairie, MN 55344, USA

Dr. Y. Shi
State Key Laboratory of Mechanics and Control of Mechanical Structures
Nanjing University of Aeronautics and Astronautics
Nanjing 210016, P. R. China

Dr. M. Han, Prof. J. A. Rogers
Departments of Materials Science and Engineering, Biomedical Engineering, Chemistry, Mechanical Engineering, Electrical Engineering and Computer Science
Center for Bio-Integrated Electronics
Simpson Querrey Institute for Nano/Biotechnology
Northwestern University
Evanston, Illinois 60208, USA

 The ORCID identification number(s) for the author(s) of this article can be found under <https://doi.org/10.1002/adem.201801254>.

DOI: 10.1002/adem.201801254

reversibly changing their dimensions upon deforming their elastomer substrates, or by tuning the amplitude of an external load.^[22] Overall, through strain-dependent vibration behavior, these structures are tunable unlike conventional MEMS devices, which mostly utilize 2D vibrational modes.

For these reasons, most 3D MEMS sensors require stretchable/flexible electronic devices to sustain repeated complex deformations imposed by either the substrate (such as the skin) or by external stimuli/loads up to 20–30% compression.^[23–25] Particularly, biological systems such as human skin undergo large elastic deformation due to their mechanical compliance. These geometrical and mechanical properties of skin have introduced challenges for designing biosensors and bioelectronics.^[26] To overcome these challenges, we have fabricated microscale 3D polymer-based kirigami architectures using patterned cuts on photo-definable epoxy (SU8), which is deposited on elastomer substrates with similar mechanical properties to the skin.^[27] The 2D layers are patterned using photolithography and reactive ion etching (RIE) in pre-stretched elastomer substrates, such as silicone. The transformation from 2D patterns into 3D engineered structures is carried out by releasing the pre-stretched material, which induces controlled compressive buckling.^[28]

The mechanical response of kirigami Si/SU8 structures to single loading was previously studied by the authors. We found that various 3D structures were resilient to large deformation, with large recoveries of nearly 90% for 100% height compression.^[29] We also found that the geometry of the 3D mesostructures plays a significant role in their flexibility and elastic recovery/resiliency. Likewise, the energy dissipated by these structures is critical, as related to cycling, as it indicates if they will be durable against repeated deformations/cycling. The behavior of these 3D architecture structures

to repeated deformation is unknown, and no reports exist in the literature on the mechanical cycling of origami- or kirigami-inspired structures.

Herein, we report on in situ SEM cyclic compression of kirigami-inspired structures, which consist of SU8. The main objective herein is to develop structures for 3D MEMS sensors with improved fatigue resistance under cyclic compression up to 50%. Thus, structures are able to maintain safe operation under 20–30% compression, thus being resilient under typical operating conditions. To understand crack formation and growth, extreme compression up to 100% was carried out on the rotated table structure. High-resolution imaging and load-displacement curves were used to monitor the onset and propagation of nano/micro-cracking within the structures. Modeling using finite element analysis (FEA) was carried out to understand the location and magnitude of stress and strain distributions at the onset of cracking. The FEA model also enabled optimization of the geometry through changes of the SU8 film thickness to make the structure more resistant to cyclic loading. Complementary tensile testing of the elastomer substrate was included to understand the influence of the substrate on the mechanical cycling of the structures.

3D architectures with different combinations of materials (polymers, metals, and semiconductors) were fabricated and successfully employed as components for devices in applications such as robotics and wearable electronics. For this study, two designs (labeled as table and rotated table) were chosen because they were found to be promising candidates for MEMS pressure/shear sensors due to their robust and simple patterns, and high elastic recovery under deformation. The 2D design patterns and their transformation into 3D architectures are shown in **Figure 1a**. The deformation of the table structures is bending-dominated, while the deformation of the rotated table is a

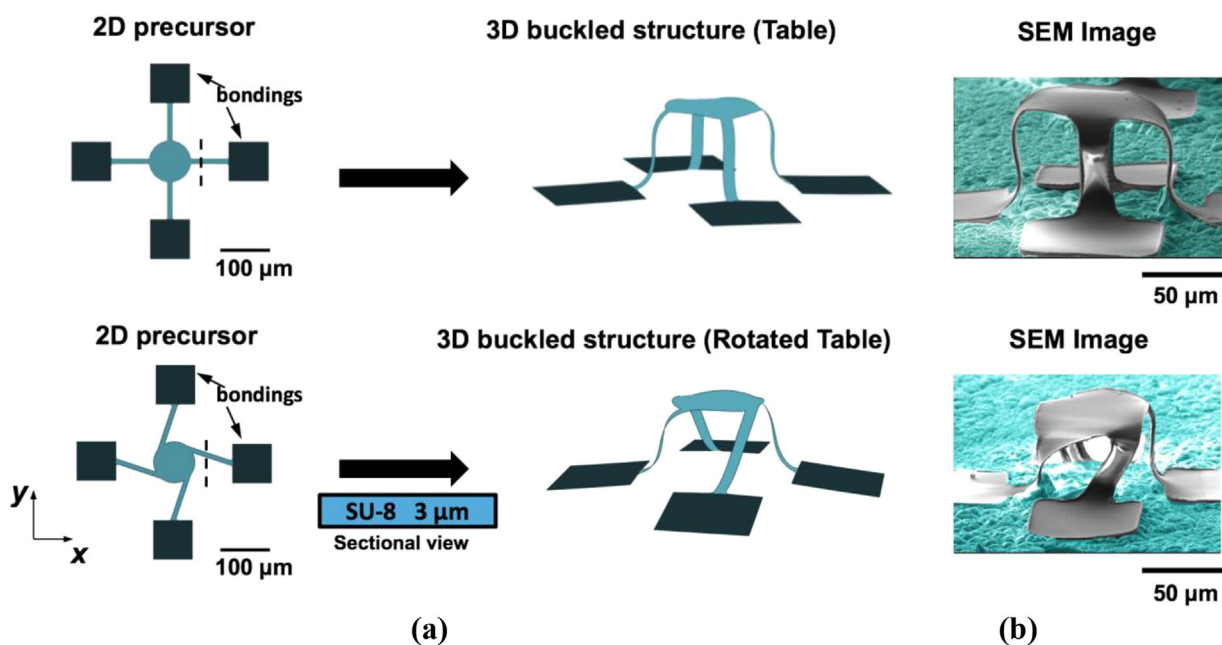


Figure 1. a) Conceptual illustration of two 3D kirigami structures, which were assembled from their 2D precursors by compressive buckling, b) corresponding SEM images of the fabricated 3D structures.

combination of bending and twisting. Another major difference between these structures is their structural stiffness, where the rotated table is three times more compliant.^[29] The kirigami structures were fabricated using a fixed pre-strain of 75%. SEM images were taken before the start of the in situ compression experiments for the assembled structures (see Figure 1b).

The compression experiments were performed using displacement-controlled loading. Compressing the structures to 50% and 100% of their initial heights are referred to as 50% and 100% compression, respectively. A contact profilometer was used to obtain precise height measurements of the structures. Figure S1 shows these two levels of compression. The samples were coated with 8 nm of Pt/Pd to provide charge dissipation during SEM characterization. SEM images in this study were colored using an open-source graphics editor (GIMP, <https://www.gimp.org/>) to enhance the contrast between the structures and the substrate. Compression experiments were carried out using different loading rates of 1, 5, and 10 $\mu\text{m s}^{-1}$ to study the loading rate sensitivity.

To understand the behavior of the silicone elastomer substrate under cyclic compression, compression experiments were carried out using a Universal Testing Machine (UTM). The substrate sample was cyclically compressed 200 times, then the load was removed for a holding period of time. This process was repeated two additional times for each sample. These tests were conducted to show the effects of strain rate, wait time, and minimum cyclical compression (see Figure S2). The slope of the curve represents the stiffness of the samples. There was no evidence of stiffening of the elastomer under cycling. The slight hysteresis in the cycling could be due to either the viscoelastic nature of the material, or due to friction between the compression platen and the sample.^[30]

Cyclic compression experiments for the elastomer substrate were carried out using the SEM indenter using the same testing conditions as for the tests of the kirigami structures. **Figure 2** shows representative load/displacement data for flat-punch compression using the SEM indenter setup. The SEM image in Figure 2 shows the location of the experiment. Each experiment consisted of 25 cycles, and the substrate was cycled at 50 and

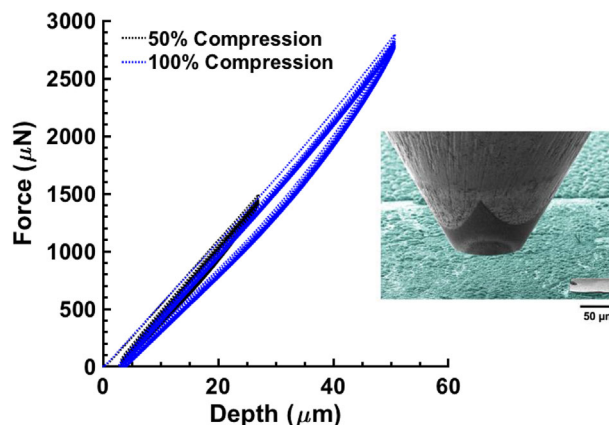


Figure 2. Load versus displacement data for flat-punch compression of the elastomer substrate.

100% height compression relative to the initial height of the structures. Cycling at 50% is recoverable and elastic with negligible hysteresis. By comparison, cycling at 100% resulted in hysteresis and dissipation. The first cycle is different than the remainder of the cycles. The hysteresis is stable and with no change in energy dissipation between cycles. The recorded movie S1 for the substrate cycling is provided in the supporting information.

To investigate the load sensitivity, single loading compression experiments with different loading rates were carried out on a rotated table structure. 50% compression was used to avoid the influence of substrate deformation at displacement rates of 1, 5, and 10 $\mu\text{m s}^{-1}$. A holding period was held at maximum displacement to investigate the creep of the structure and substrate under the applied displacement. **Figure 3a** shows a slight rate-sensitivity on the loading stiffness, where faster loading rates minimize the rate sensitivity. The 1 $\mu\text{m s}^{-1}$ experiments were conducted as the last set of experiments; therefore, the difference could be due to the non-complete relaxation of the substrate. Experiments with 10 and faster rates

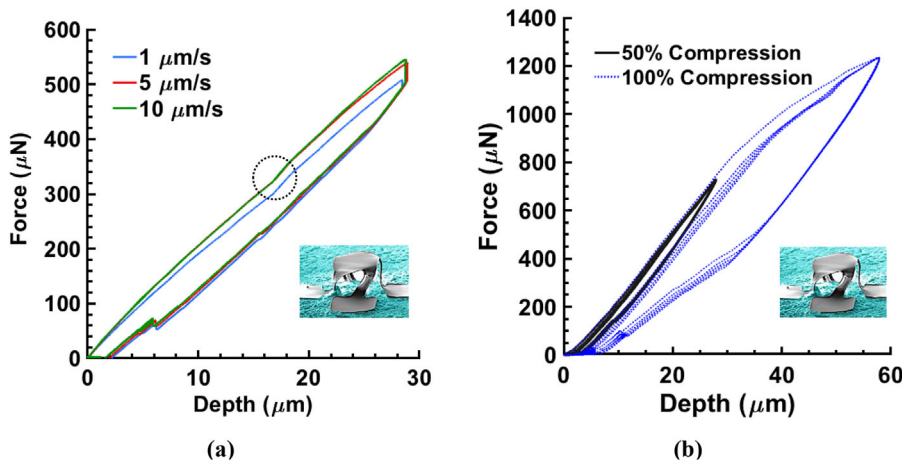


Figure 3. a) Loading rate study at 50% compression, b) representative load versus displacement data for 50% and 100% height compression (5 cycles shown here).

of $25 \mu\text{m s}^{-1}$ (for large number of cycles) were adopted in this work for the table and rotated table structures, respectively. Supplementary movies S2 and S3 are provided for experiments with 1 and $10 \mu\text{m s}^{-1}$ loading rates.

The load-displacement curves in Figure 3a revealed that the discontinuity in the loading part at nearly 30% compression ($\approx 20 \mu\text{m}$, highlighted with a circle) is due to the activation of twisting deformation in the legs (See Supplementary movies S2 and S3). Earlier, a linear bending-dominated deformation was observed. Similar discontinuity is observed in the unloading part at the same depth. Additionally, the unloading part shows a snap at the end of the experiment as the indenter withdrew from the structure.

Compressing structures to 50% and 100% revealed different cycling behaviors. Figure 3b provides a comparison between 5 compression cycles at 50% and 100% on a single rotated table structure to assess repeatability and recoverability. The structure maintained very low and stable hysteresis under 50% compression. The compression was linear and the deformation was bending dominated. No significant difference was observed between the first cycle and subsequent cycles. Upon the removal of the load, the structure recovered completely. This was confirmed by compressing the same structure again up to 100%.

Interesting phenomena were observed during the extreme 100% compression. The first cycle is similar in behavior (shape) to the subsequent cycles but with higher dissipated energy. Next, while there is shifting of load–displacement curves, there is no change in the energy dissipation after the first cycle. Also, the unloading behavior is composed of the recovery of both substrate-structure bending deformation and the recovery of the twisting deformation of the structure. The unloading behavior can be divided to reflect these two segments. All cycles have similar deformation during the first one-third of the unloading. In this region, the substrate dominates the response due to the higher stiffness, which leads to faster and earlier recovery of the substrate. In the second region (final two-thirds of unloading), the structure further recovered, mainly due to untwisting and also showing some creep behavior.

Profilometric measurements were performed after cycling the structure to 100% to precisely measure the residual deformation. The residual deformation is about $4 \mu\text{m}$, thereby resulting in 94% elastic recovery (see Figure S3). The different energy

dissipation in the first cycle could be attributed to plastically deforming the structure, whereas the next cycles showed less plastic deformation. Figure S4 provides a comparison of the flat-punch compression of the substrate and the rotated table structure highlighting more nonlinear and compliant deformation of the structure as compared to compressing the substrate alone.

Figure 4a illustrates the cycling of the table structure at 50% compression. 30 cycles were carried out and were divided into three sets, where each set consists of 10 cycles. Four minutes was set as a wait time to allow relaxation of the structure and substrate before carrying out the next set of cycling. A recorded movie for the first set is provided in the supporting information (See movie S4). After each set, complete unloading was carried out followed by a period of 4 min to allow complete relaxation of both the structure and the substrate. The load displacement curves show complete recovery between sets, which is illustrated by the overlap of the loading and unloading parts of the compression data. The structure experienced minimal and stable hysteresis with no accumulation over succeeding cycles. The shifting of the hysteresis cycles downward could be due to the creep of either the substrate or structure. Figure 4b shows SEM images at higher resolution, taken before and after the 3 cycling sets. The cycling compression at 50% is fully recoverable with no change in the shape of the structure or observable plastic deformation/cracks. Due to the linear and elastic behavior, no additional cycling tests were performed at 50% compression. Similar linear behavior is observed for bistable electroactive polymers (BSEP) when cycled at 50% compression.^[31]

Cycling experiments for a rotated table structure were conducted at 100% compression. The goal is to evaluate its resilience under extreme (to-failures) loading conditions far beyond their engineering application range of 20–30% compression. Eight sets were carried out, and each set consisted of 25 cycles (200 total cycles). The same wait time of 4 min between sets was used. Figure 5a and b shows the 8 sets divided into two figures for clarity. Also, each figure shows distinct deformation behavior due to the transition event at the end of the fourth set. In Figure 5a, the first cycle dissipated larger energy and the deformation was more non-linear, as compared to the subsequent cycles. The structure achieved post-buckling/twisting stability after the second cycle. The first cycles of the next three

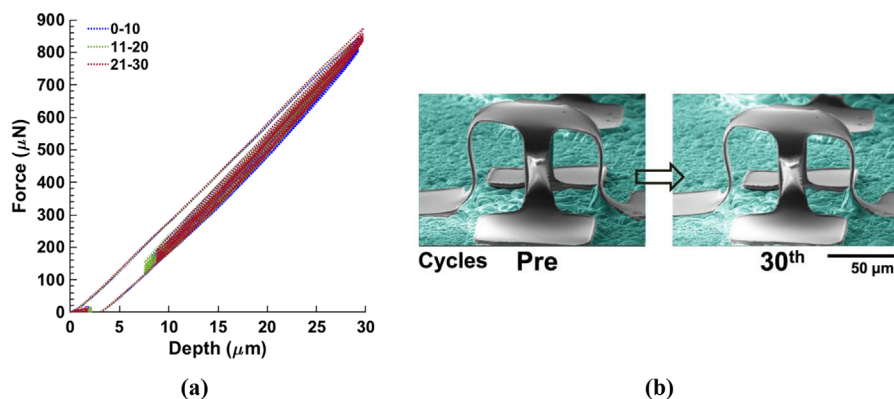


Figure 4. a) Load versus displacement for cycling of a table structure to 50%. b) SEM images taken before the experiment and after the 30th cycle.

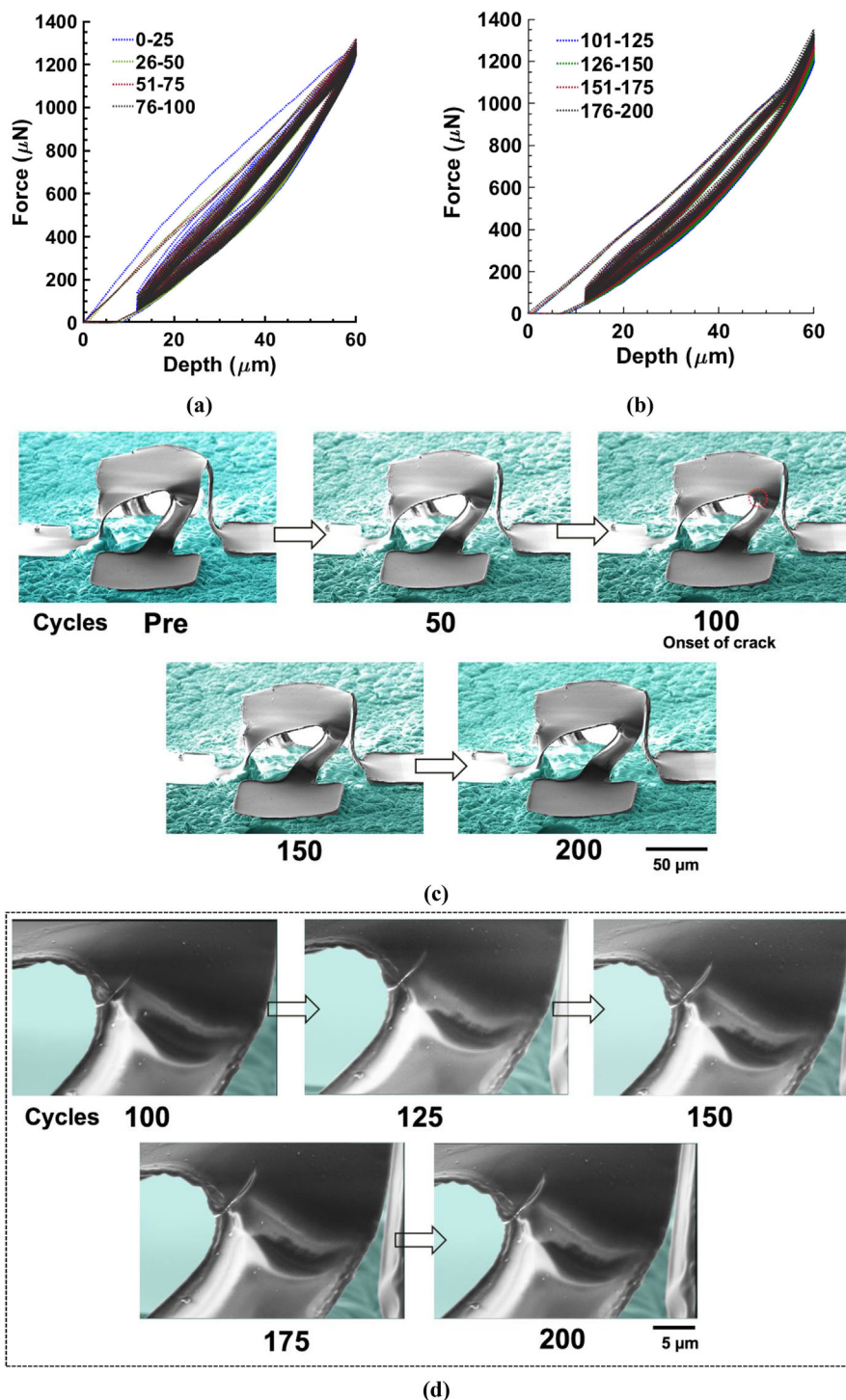


Figure 5. Load versus displacement for cycling of a rotated table structure at 100% compression: a) 0–100 cycles. b) 101–200 cycles. c) SEM images taken before the start of compression and after different sets of cycles (only every other set is provided here). The dashed circle in the SEM image after 100 cycles highlights the location of the generated microcrack. d) Close-up SEM images providing the growth rate and direction of the microcrack shown in the dashed circle in (c).

sets showed similar linear responses. The results also show that the structure tends to deform more linearly with less hysteresis with increasing cycling. A reduced vibrational nonlinearity was observed in a previous study for these structures under high amplitude of external loading.^[22]

Figure 5b reveals a sudden change in the behavior of the structure starting from the 5th set (>100th cycles). First, the hysteresis was reduced showing more stable cycling with less change between cycles. Furthermore, the loading part of the deformation became linear. The generation of a microcrack at

the beginning of this set could explain this change in behavior. Indeed, the SEM images in **Figure 6a** and **b** reveal the initiation of a crack in one of the membrane-ribbon connections.

There was a slight stiffening as the structure is compressed to nearly 100% compression after the 5th set, shown in **Figure 5b**. The mechanism behind this stiffening is shown clearly using high resolution SEM images and the supporting information (Movies S5–S6). The recorded Movie S5 is for the first set, while the Movie S6 is for the last set. Upon compression to 100%, sliding and twisting of the structure occurred and became larger after the generation of the micro-crack. The height of the structure remained similar, however, it twisted out of the x - y plane. Therefore, when compressed again, the legs of the structure compressed against its bonding pads showing stiffening behavior. Movie S6 clearly revealed this nonlinear compression of the leg of the structures for cycles 176–200.

To better understand the structural shape changes under mechanical cycling, superposition of SEM images before compression and after the end of mechanical cycling is shown in **Figure 6**. The dashed black line represents the initial shape, while the solid red line indicates the final shape of the structure after cycling. The cycling to 50% compression was elastic and recoverable with no obvious shape changes of the structure. Also, no sliding of the structure was observed. By comparison, cycling to 100% showed a change in the shape of the structure through a slight combination of sliding and twisting of the structure to the right in the direction of the microcrack growth. The sliding could have occurred due to the tilting surface of the rotated table structure or the interfacial adhesion and friction between the flat punch and the top of the structure. The indenter/structure sliding is noticeable in Movies S5 and S6. The sliding of the rotated table structure at 100% compression contributed to the higher hysteresis, as compared to the table structure (at 50% compression) and potentially to the introduction of microcracks.

Based on classical plate theory, the shape of structures under buckling is a function of the aspect ratio (width to thickness ratio), applied loading, and boundary conditions.^[32] To prevent or delay the initiation of cracks and provide higher design factor of safety, a better understanding of stress/strain distributions was carried out using FEA. These models were also used to optimize the SU8 thickness to mitigate local stress

concentrations. **Figure 7** illustrates a comparison of the FEA with the experimental results by comparing snapshots from the recorded movies to the FEA deformation. The FEA modeled only a single compression due to the challenges in computational modeling of cyclic loading, which includes material parameters being determined or fitted using empirical laws, such as Paris' law.

Figure S5 and **8** show the von Mises stress and maximum principal strain contours for table (compressed to 50%) and rotated table (compressed to 100%) structures. The substrate and punch were removed to allow visual observation of the stress and strain contours in the structures. The SU8 thickness (t) was varied from 500 nm to 4 μm in the FEA model. 500 nm represents the minimum thickness of SU8 film that can be spin-coated. For both structures, reducing the SU8 thickness results in reduced von Mises stresses and principal strains in the legs of the structures. Also, the deformation mode changes from bending-dominated to buckling-dominated as the thickness is reduced, thus showing more compliant behavior. Furthermore, the substrate effect is reduced showing more compliant behavior (less stiffness) for the structures.

The in situ SEM experiments were carried out using structures with SU8 thickness of 3 μm . For the rotated table structure, reducing the SU8 thickness from 3 to 1 or 2 μm reduces the stress concentrators at the membrane-ribbons location (see **Figure 8**). These locations correspond to the site of crack nucleation. Therefore, the reduction of SU8 thickness provides a design route to eliminate the formation of microcracks to achieve higher safety factors. Another potential material route is to use more compliant substrates or different photoresist materials for the structures, both which were not studied in this work.

The unloading stiffness was measured from the FEA by dividing the maximum load over the maximum displacement at the onset of unloading. The maximum load bearing and unloading stiffness were measured at 50% compression for both structures to avoid substrate effects. A change in the stiffness would lead to a slight change in the linear natural frequency. The resonance frequency is a function of effective stiffness and mass. Thus, changing the SU8 thickness can produce a change of the bandwidth of sensors or vibrational micro-platforms. An advantage exists from an application point of view for having

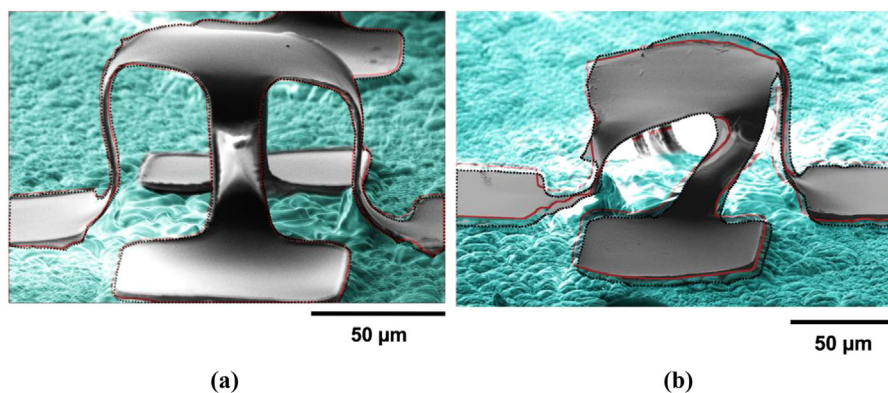


Figure 6. Superimposed images for table (pre-compression and 30th cycle) and rotated table structures (pre-compression and 200th cycle).

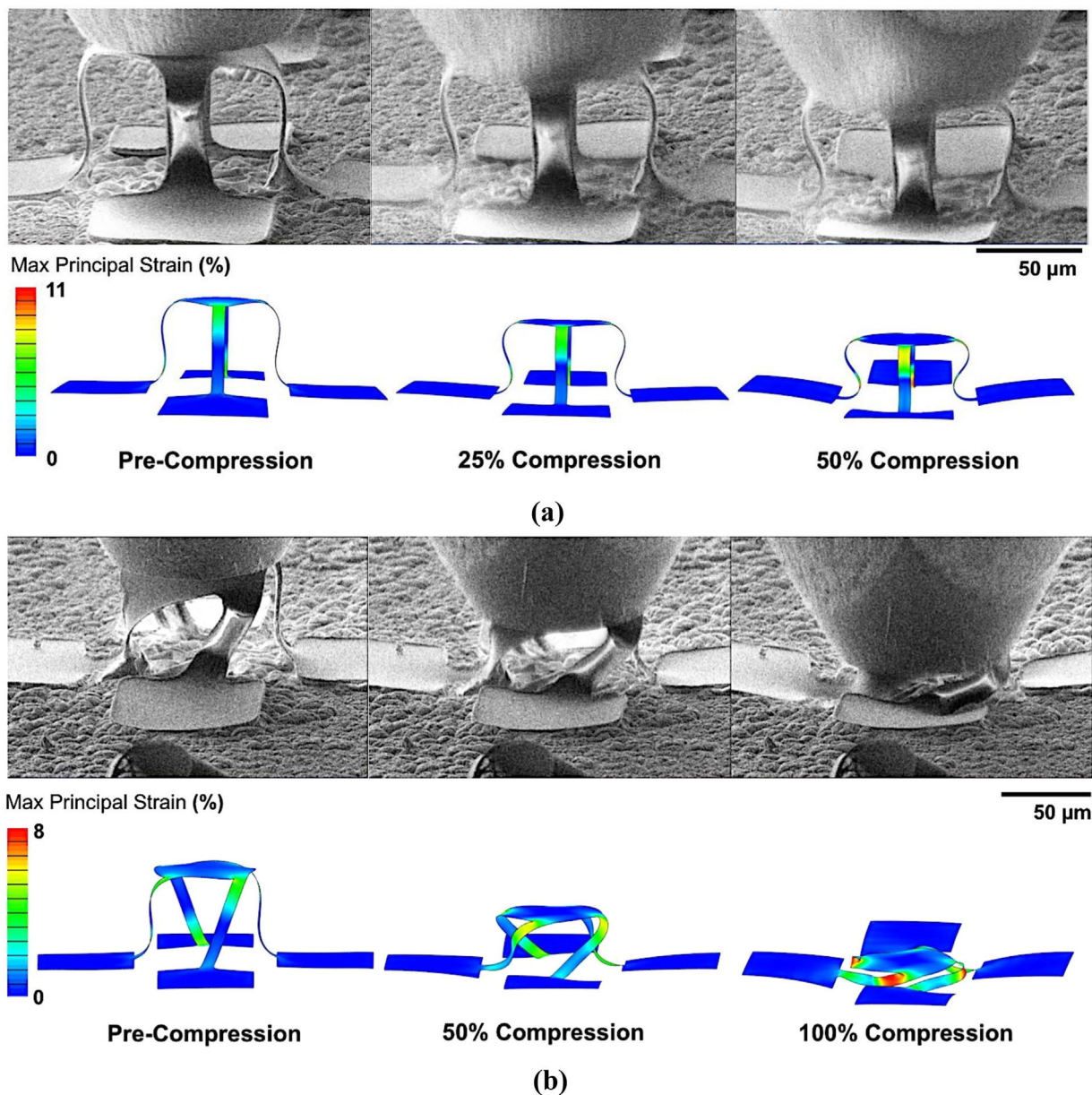


Figure 7. Snapshots taken from the recorded movies (during the 1st cycle) and the FEA at different percentages of height compression for the (a) table and (b) rotated table structures.

frequency tunability since it can improve the detection ranges for mass sensing.^[33,34] The effective stiffness is proportional to the equivalent modulus, total thickness, and inversely proportional to lateral length.^[35] While the modulus is a material factor, the remainder are geometrical factors, which could be optimized using FEA to further improve the frequency of these devices, and their resilience against mechanical deformation.^[36]

Table 1 provides a comparison for both structures in terms of different SU8 thickness. The maximum load and unloading stiffness decrease for structures with smaller SU8 thicknesses as the structures become more compliant. Reducing SU8 thickness from 4 to 1 μm results in reduction of the load bearing capability by nearly a factor of 10 for both structures. Similar findings are

observed for the unloading stiffness. Changing the SU8 thickness can produce structures with different stiffness. This enables the opportunity to tune MEMS pressure/shear sensors to achieve specific sensing capabilities. Also, Table 1 offers design guidelines for the selection of structures' thickness, based on the requirements and loading conditions imposed by the application.

The reliability against compressive cycling is critical for soft MEMS biosensors such as pressure and shear sensors. Such applications might be subjected to compression up to 20–30%. Cycling at 50% of the height of the structure was found to be completely elastic and maintained stable hysteresis during cycling. Therefore, the kirigami structures were found to provide

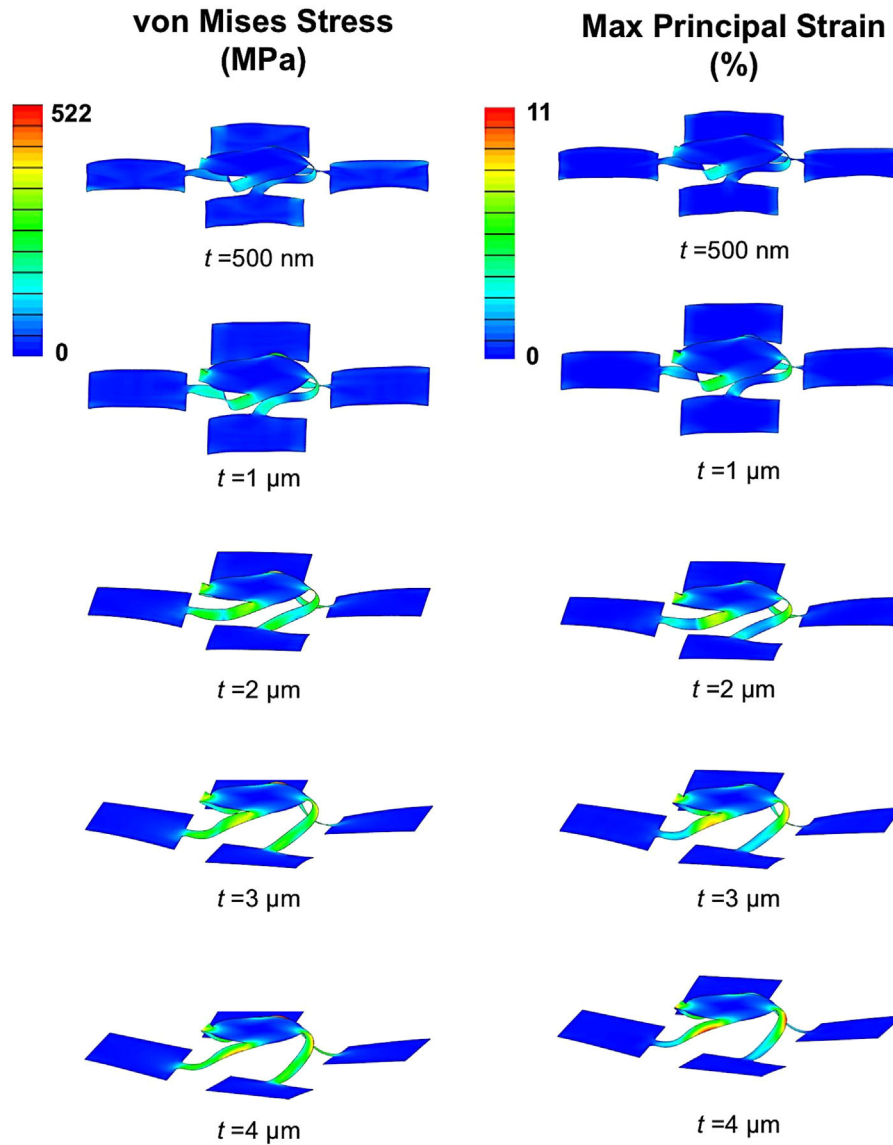


Figure 8. FEA results for a single compression of SU-8 kirigami rotated table structures (under 100% compression) showing von Mises stress (MPa, left column) and maximum principal strain (right column) for different SU8 thickness.

reliable operation for these MEMS devices. To further improve their toughness beyond the applications' requirements and understand their failure mechanics, a more extreme cycling at 100% of the height was carried out, and the structure showed 94% elastic recovery with high hysteresis during the first few cycles. After few cycles, the structures reached stable hysteresis. The FEA model showed that the structures had a maximum principal strain approaching the max strain to fracture for SU8 ($\approx 12\%$). These large strains accompanied by sliding of the structure caused a crack to initiate at the 100th cycle, and the crack continued to grow slowly under the cyclic stress. The crack propagation is stable and the structure maintained stable hysteresis. A reduction of SU8 film thickness can provide a design route to eliminate microcrack formation and further increase the design factor of safety. Future studies will address the influence of packaging on the mechanics of these structures.

Often, packaging is required to prevent corrosion and achieve biocompatibility of inorganic materials such as silicon and metal oxides operating in contact with the skin or inside the human body.

2. Experimental Section

2.1. Materials and Fabrication

The fabrication started with spin coating SU-8 ($3\ \mu\text{m}$ thickness) on top of a thin layer of SiO_2 ($800\ \text{nm}$ thickness), which is deposited on a Si wafer. Then, photolithography and reactive ion etching created the pattern of the 2D precursor layout. To dissolve the exposed SiO_2 , wet etching by hydrofluoric acid (HF) was used. A second sacrificial layer of $4\ \mu\text{m}$ photoresist (AZ

Table 1. Comparison between table and rotated table structures in terms of response to mechanical deformation with different SU8 thickness (based on FEA model).

Table		
Thickness (μm)	Maximum load bearing [μN]	Unloading stiffness [N m^{-1}]
0.5	21	0.53
1	133	3.36
2	584	14.43
3	1040	23.96
4	1390	28.25
Rotated table		
Thickness (μm)	Maximum load bearing [μN]	Unloading stiffness [N m^{-1}]
0.5	6	0.15
1	58	1.43
2	220	5.42
3	462	10.95
4	664	14.65

5214) was deposited on top of the pattern except at the bonding sites. HF wet etching was used to fully remove the SiO_2 beneath the pattern. This allowed for transfer printing of the 2D precursor from the Si wafer to the elastomer substrate.

To improve adhesion between the bonding regions of the structures and the elastomer substrate, an ultra-thin layer of titanium (5 nm thickness) followed by a layer of silicon dioxide (50 nm thickness) were deposited using electron beam evaporation. A polydimethylsiloxane (PDMS) stamp was used to lift the precursors from the wafer to a water soluble polyvinylalcohol (PVA) tape. A “Dragon Skin” elastomer (Smooth-On, Macungie, PA, 600 μm thickness) was used as a substrate for the buckling process. The silicone elastomer was stretched using a custom stage up to 75% prestrain. To promote strong bonding, both the substrate and the 2D precursors on the water-soluble tape were subjected to ultraviolet ozone treatment to induce hydroxyl termination. Then, the tape was laminated to the substrate followed by heating at 70 °C for 8 min to form strong chemical bonding between the bonding regions of the 2D precursors and the silicone elastomer via condensation reactions. The water-soluble tape and AZ 5214 layer were dissolved using water and acetone, respectively. The non-bonding regions became weakly bonded with Van der Waals forces to the substrate after the removal of the AZ 5214 layer. Releasing the prestrain of the silicone substrate induced out-of-plane translations of the non-bonding regions.

2.2. Mechanical Characterization

The in situ SEM cyclic compression experiments were carried out using a PI 88 SEM PicoIndenter (Bruker Nano Surfaces, Eden Prairie, MN). To allow large displacement up to 150 μm , the extended range (xR) transducer was used with this setup. A diamond flat punch (100 μm in diameter) was used to compress the structures.

2.3. Finite Element Analysis

Three-dimensional (3D) finite element analysis (FEA) was employed to predict the final configurations and stress/strain distributions of the 3D structures using the commercial software ABAQUS. Four-node shell elements and eight-node 3D stress elements were adopted to simulate the kirigami structures and the elastomer substrates, respectively. Convergence of mesh sizes ensured computational accuracy. The elastomer substrate was modeled using a hyperelastic constitutive relation (Mooney-Rivlin model) with parameters $C_{10} = 0.06757 \text{ MPa}$, $C_{01} = 0.01689 \text{ MPa}$, and $D_1 = 0.48 \text{ MPa}^{-1}$ in ABAQUS. The elastic moduli (E) and Poisson’s ratios (ν) for SU-8 were taken as $E_{\text{SU-8}} = 4.02 \text{ GPa}$ and $\nu_{\text{SU-8}} = 0.22$.

Supporting Information

Supporting Information is available from the Wiley Online Library or from the author.

Acknowledgements

Funding of this study was provided from the Hagler Institute for Advanced Study (HIAS) at Texas A&M University. C. D. Fincher was supported by the National Science Foundation Graduate Research Fellowship under Grant No. 1746932. Y. Shi thanked the support from National Natural Science Foundation of China (Grant No. 11702131). The authors acknowledged the help of Zhi Li in the computational modeling.

Conflict of Interest

The authors declare no conflict of interest.

Keywords

cycling, fatigue, kirigami, resilient, 3D microstructures

Received: November 23, 2018

Published online:

- [1] K. R. Jayne, J. T. Stark, B. J. Reeves, J. D. Bishop, E. A. White, *Adv. Mater. Technol.* **2018**, 3, 1700293.
- [2] B. Sun, H. D. Asfaw, D. Rehnlund, J. Mindemark, L. Nyholm, K. Edström, D. Brandell, *ACS Appl. Mater. Interfaces* **2018**, 10, 2407.
- [3] R. Clark, K. Tapily, K.-H. Yu, T. Hakamata, S. Consiglio, D. O’Meara, C. Wajda, J. Smith, G. Leusink, *APL Mater.* **2018**, 6, 58203.
- [4] Y. Wang, Y. Qiu, S. K. Ameri, H. Jang, Z. Dai, Y. Huang, N. Lu, *npj Flex. Electron.* **2018**, 2, 6.
- [5] K. J. Hoon, K. D. Chan, S. H. Joon, K. Tae-Ho, K. Dae-Hyeong, *Adv. Funct. Mater.* **2018**, 0, 1801834.
- [6] S. Han, J. Kim, S. M. Won, Y. Ma, D. Kang, Z. Xie, K.-T. Lee, H. U. Chung, A. Banks, S. Min, S. Y. Heo, C. R. Davies, J. W. Lee, C.-H. Lee, B. H. Kim, K. Li, Y. Zhou, C. Wei, X. Feng, Y. Huang, J. A. Rogers, *Sci. Transl. Med.* **2018**, 10, Article ID 4950.
- [7] K.-G. Noh, S.-Y. Park, *Adv. Funct. Mater.* **2018**, 28, 1707562.
- [8] S. Nakata, T. Arie, S. Akita, K. Takei, *ACS Sensors* **2017**, 2, 443.
- [9] H. L. and M. D. and N. F. and N. L. and P. R. and P. Vettiger, *J. Micromech. Microeng.* **1997**, 7, 121.
- [10] Y. Liu, K. He, G. Chen, W. R. Leow, X. Chen, *Chem. Rev.* **2017**, 117, 12893.

- [11] C. Wang, L. Taherabadi, G. Jia, M. Madou, Y. Yeh, B. Dunn, *Electrochem. Solid-State Lett.* **2004**, *7*, A435.
- [12] M. M. and I. H. and A. D. L. and J. C. and F. Udrea, *J. Micromech. Microeng.* **2018**, *28*, 85013.
- [13] A. C. R. Grayson, R. S. Shawgo, A. M. Johnson, N. T. Flynn, Y. Li, M. J. Cima, R. Langer, *Proc. IEEE* **2004**, *92*, 6.
- [14] E. Mounier, News market perspectives for the MEMS & sensors. *Yole Developpement* **2018**, 1–4, http://www.yole.fr/MEMS_Market.aspx#_XB_EpC2ZNP9 (accessed: July 2018).
- [15] J. Rogers, Y. Huang, O. G. Schmidt, D. H. Gracias, *MRS Bull.* **2016**, *41*, 123.
- [16] J. Iannacci, *Displays* **2015**, *37*, 62.
- [17] V. Mulloni, B. Margesin, P. Farinelli, R. Marcelli, A. Lucibello, G. De Angelis, *Microsyst. Technol.* **2017**, *23*, 3843.
- [18] M. Tanaka, *Microelectron. Eng.* **2007**, *84*, 1341.
- [19] M. T. Jan, N. H. B. Hamid, M. H. Md Khir, K. Ashraf, M. Shoaib, *J. Qual. Reliab. Eng.* **2014**, 2014.
- [20] X. Ning, H. Wang, X. Yu, J. A. N. T. Soares, Z. Yan, K. Nan, G. Velarde, Y. Xue, R. Sun, Q. Dong, H. Luan, C. M. Lee, A. Chempakasseril, M. Han, Y. Wang, L. Li, Y. Huang, Y. Zhang, J. A. Rogers, *Adv. Funct. Mater.* **2017**, *27*, 1605914.
- [21] C. Munkelt, M. Heinze, T. Zimmermann, P. Kühmstedt, *Proc. SPIE* **2018**, *10667*, 1066706.
- [22] H. Wang, X. Ning, H. Li, H. Luan, Y. Xue, X. Yu, Z. Fan, L. Li, J. A. Rogers, Y. Zhang, Y. Huang, *J. Mech. Phys. Solids* **2018**, *112*, 187.
- [23] V. Coskun, B. Ozdenizci, K. Ok, *Sensors* **2015**, *15*, 13348.
- [24] Y. Shi, P. Pei, X. Cheng, Z. Yan, M. Han, Z. Li, C. Gao, J. A. Rogers, Y. Huang, Y. Zhang, *Soft Matter* **2018**, *14*, 8828.
- [25] D. H. Alsem, O. N. Pierron, E. A. Stach, C. L. Muhlstein, R. O. Ritchie, *Adv. Eng. Mater.* **2007**, *9*, 15.
- [26] J. Coffel, E. Nuxoll, *Int. J. Pharm.* **2018**, *544*, 335.
- [27] Y. Zhao, X. Huang, *Micromachines* **2017**, *8*, 69.
- [28] B. Xu, J. A. Rogers, *Extrem. Mech. Lett.* **2016**, *7*, 44.
- [29] H. Mohammad, S. Yan, H. Mengdi, L. Joseph, Y. Zheng, P. Matt, Z. Yihui, H. Yonggang, R. A. John, P. A. Andreas, *Small* **2018**, *14*, 1703852.
- [30] R. B. Bird, B. D. Marsh, *Trans. Soc. Rheol.* **1968**, *12*, 479.
- [31] Y. Xie, Y. Meng, W. Wang, E. Zhang, J. Leng, Q. Pei, *Adv. Funct. Mater.* **2018**, *0*, 1802430.
- [32] P. E. Fenner, A. Watson, *Thin-Walled Struct.* **2012**, *59*, 171.
- [33] N. Xin, W. Heling, Y. Xinge, S. T. N. A. Julio, Y. Zheng, N. Kewang, V. Gabriel, X. Yeguang, S. Rujie, D. Qiyi, L. Haiwen, L. C. Mi, C. Aditya, H. Mengdi, W. Yiqi, L. Luming, H. Yonggang, Z. Yihui, R. A. John, *Adv. Funct. Mater.* **2017**, *27*, 1605914.
- [34] L. Yu, H. Shahsavan, G. Rivers, C. Zhang, P. Si, B. Zhao, *Adv. Funct. Mater.* **2018**, *0*, 1802809.
- [35] W. Li, W. Zhang, H. Zou, Z. Peng, G. Meng, *Smart Mater. Struct.* **2017**, *26*, 85033.
- [36] R. M. Neville, F. Scarpa, A. Pirrera, *Sci. Rep.* **2016**, *6*, 31067.